Progress In Electromagnetics Research C, Vol. 116, 129–144, 2021

Improved Neighborhood-Based Algorithm to Facilitate the Reduction of Skin Reflections in Radar-Based Microwave Imaging

Michael R. Smith[1, 2, *] and Elise Fear[1]

Abstract—Low power, near-field (NF) radar imaging techniques have been proposed for breast cancer detection and long-term monitoring. It is important to optimize the data processing paths required for NF image reconstruction given the inherent resolution limitations of microwave compared to MRI or X-ray imaging. A key limitation in obtaining internal tumour and breast feature information is the reflection from the skin surface physically close to the antenna. Typically, algorithms to remove this dominant reflection involve subtracting an estimate of the time domain signal for the skin reflection from one antenna location using information from other locations. A key challenge in these approaches is determining the portion of the signal, the skin dominant window (SDW), to use to determine the weights applied to nearby antenna signals when calculating the skin reflection estimate. Equipment limitations and breast characteristics impact the amount of data that can be captured, leading to the well-known Gibbs' ringing distortions in the time domain signals. We suggest that the Gibbs' ringing from the magnitude larger skin reflection has caused the length of the SDW to be over-estimated in previous determinations. Since this distorted signal now overlaps the time signals from the tumour and breast responses, removing the skin reflection estimate may result in attenuation of tumour responses. In this contribution, two alternative strategies for designing the SDW are proposed. One minimized the first skin peak in the SDW, i.e., the furthest from the breast feature signals, and the other minimized the main, i.e., largest, skin peak within the SDW. Both new approaches were shown to effectively suppress the skin signal on simulated and patient data while allowing recovery of the missing portions of the desired internal breast feature signals leading to an increase in the overall intensity of the images and preserving the tumour response. However, we provided reasons why we considered that basing the suppression on the largest skin signal peak would provide a more consistent improvement in the breast feature signals.

1. INTRODUCTION

In comparison with X-ray based mammography, there are advantages in using low-power, non-ionizing microwaves for imaging when repeated monitoring is required to follow changes in cancerous breast tissue [1]. Reflected signals are captured from multiple locations around the breast using multi-static, e.g., [2], or monostatic approaches, e.g., [3]. Image contrast relies on the differences in the dielectric properties of malignant and normal tissues encoded in the 1D frequency information captured from each antenna position.

Microwave imaging is inherently lower resolution than X-ray or magnetic resonance imaging, MRI. To avoid unintentionally introducing further image degradation, it is important that the reflection signals from individual antenna are optimized before being combined into a 2D or 3D representation of the breast tissue properties using a Delay-and-Sum reconstruction algorithm [4, 5]. A major optimization

Received 26 May 2021, Accepted 26 September 2021, Scheduled 12 October 2021

* Corresponding author: Michael R. Smith (Mike.Smith@ucalgary.ca).

[1] Department of Electrical and Software Engineering, Schulich School of Engineering, University of Calgary, T2N 1N4, Canada.

[2] Department of Radiology, Cumming School of Medicine, University of Calgary, T2N 4N1, Canada.

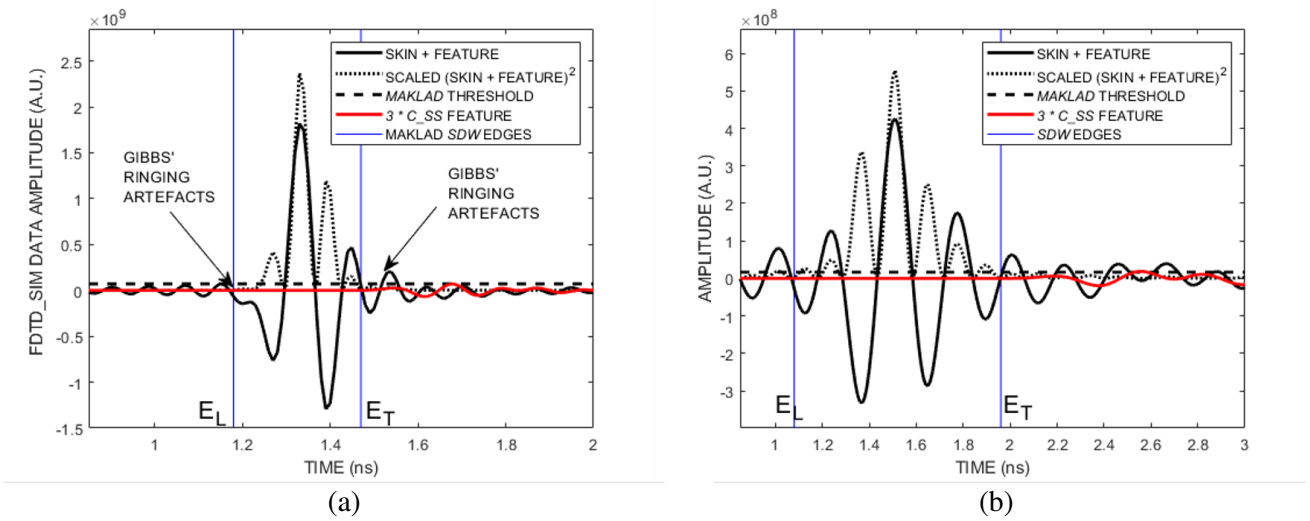

Figure 1. The leading and trailing edges, E_L and E_T, denote the extent of the Maklad skin dominant window (SDW) in these time domain signals from (a) a simulation study, and (b) a patient study. Generating these time signals by transforming the captured bandlimited frequency domain signal using the DFT introduces Gibbs' ringing distortions. These are present throughout the time domain signal, arrows, being most clearly evident in the region prior to the arrival of the first true signal reflected from the skin surface. These ripples can distort the determination of the SDW limits as can be seen at the SDW leading edge in Figure 1(a). In addition, we suggest that the Gibbs' ringing associated with strong skin reflection signal frequently overlaps the true weaker tumour signal in the region around E_T. Thus removal of the skin reflection will modify, i.e., distort, the tumour signals.

challenge is that the strength of the reflections from the skin physically near the antenna aperture, Figure 1 black line, is more than an order of magnitude stronger than reflections from small features internal to the breast, shown as the red line scaled by 3, in the time signals from both the (a) simulation and (b) patient studies.

Removing the dominant skin reflection with a data adaptive algorithm was proposed by Bond et al. [6]. This algorithm was updated by Maklad et al. [7] to automatically identify the portion of the signal dominated by the skin reflection, the skin dominant window SDW. Tumour and feature detection was then improved by computed skin subtraction, C_SS, i.e., subtracting a skin reflection estimate calculated using a weighting of reflections from antennas neighbouring the target antenna. The weighting coefficients were determined by minimizing the differences between the true and estimated skin reflections within the SDW.

When using simulated data, we determined that the early breast feature components of the C_SS result were significantly less intense than equivalent data sections following an ideal skin subtraction, I_SS. A brief empirical investigation showed that moving the trailing edge of the SDW, E_T, to cause a small decrease in the original SDW width resulted in a closer match between I_SS and C_SS results. This suggests that the direct application of Maklad approach to correct the skin reflection causes an overestimation of the SDW width. This paper explores the reasons why the SDW width may be incorrectly determined and proposes alternative approaches to determining an SDW that improves the match between ideal and computed images following skin reflection removal.

This paper is organized as follows. An overview of NF radar imaging is provided in Section 2, with specific reference to the current algorithm for removing the skin reflection signal. Section 3 details the simulation and patient data used in this study and outlines proposed modifications to SDW determination to decrease the differences between ideal and computed skin subtraction. Section 4 details a comparison of the results from the original and proposed C_SS algorithms in the context of NF studies using tissue sensing sensitive adaptive radar, TSAR. This is followed by a conclusion and suggestions of future research directions.

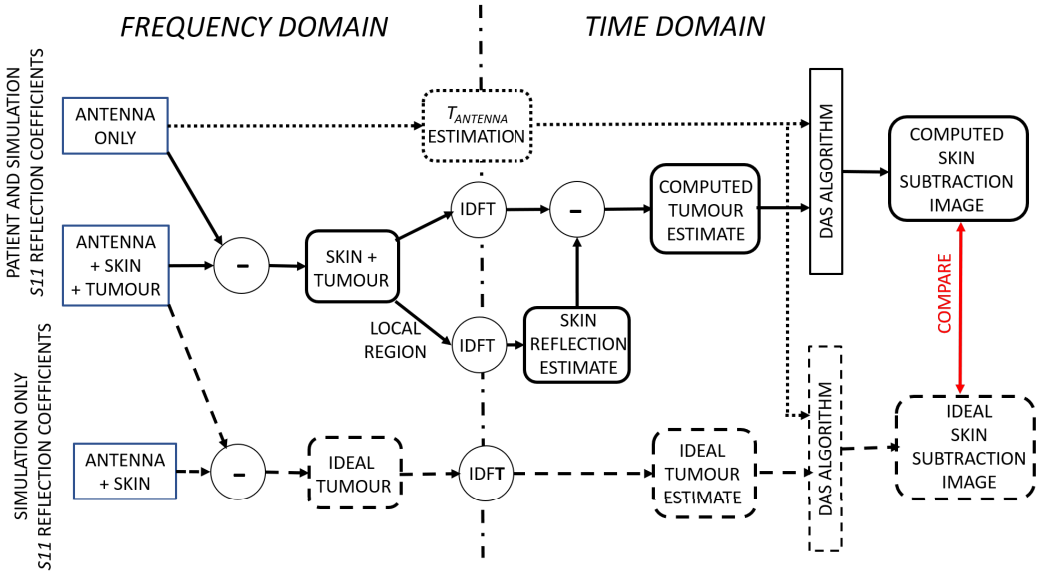

Figure 2. Schematic of the preprocessing flow (upper solid path) that generates the computed skin subtraction image from the antenna-only and antenna-skin-tumour frequency domain signals. The ideal skin subtraction image (lower dashed path) formed from the antenna-skin-tumour and antenna-skin signals is not available for the patient studies. The upper dotted path indicates that an estimation of the antenna feed to aperture transit time, T_{ANTENNA}, is required to correctly position the information encoded in the 1D time signal, Figure 1, within the 3D image scatter spaces.

2. NEAR-FIELD RADAR IMAGE RECONSTRUCTION

In this section we briefly outline the capture of the TSAR frequency information and the data-processing required to generate the near-field radar image discussed in greater detail in [4, 5, 8, 9]. We provide a theoretical explanation of why the SDW width may be incorrectly determined with the Maklad algorithm and how this impacts the voxel intensities in the final NF image. Figure 2 provides a flowchart outlining the stages of processing the captured patient or simulated 1D frequency data from individual antennas into 3D images, and a comparison path, in red, used to validate the new proposed SDW determination methods.

2.1. Data Capture and Skin Reflection Removal

The woman to be scanned lies prone on a table with her breast in a scanning tank. A vector network analyzer is used to determine the complex reflection coefficients (S_{11}) of the microwave signals, $F\_\text{Scatter}_m[n\Delta F]$; $1 \leq m \leq M$, reflected from the breast over the frequency range $F_{\text{RANGE}} = 10\,\text{MHz}$ to 8–12 GHz in $\Delta F = 10\,\text{MHz}$ steps at M antenna positions around the breast. Internal reflections from the antennas are suppressed by subtracting signals obtained from an empty scanning tank at the same antenna positions, solid line Figure 2.

This modified 1D frequency domain patient data from an individual antenna is transformed into the time domain, $T\_\text{Scatter}_m[n\Delta T_{\text{ICZT}}]$, Figure 1 black line, using an inverse discrete Fourier transform, IDFT. Next, an estimate of the skin reflection is removed. The following summarizes the computed subtraction of the dominant skin reflection using the Maklad process [7] updated from [6]. The extent of the skin dominant window, SDW, is identified by locating the significant local maxima (peaks) and minima (troughs) present in the power of the time signal, dotted black line. The troughs in the power signal correspond to the zero-crossings in the original time signal with an accuracy of $\pm\Delta T_{\text{ICZT}}$ when the IDFT is implemented via the inverse chirp Z-transform, ICZT. The SDW's leading edge, E_L, is set as the closest time step associated with the trough preceding the first significant skin reflection peak,

first blue line. The trough following the last significant peak is identified as the SDW's trailing edge, E_T, second blue line. A threshold of 3% of the maximum power level [7], dashed black line, is used to identify which power peaks are to be considered significant enough to contribute to the SDW. A specific SDW is established for each antenna. This is particularly important in the patient studies as the physical characteristics of the skin (e.g., thickness) are not anticipated to be the same at different locations around the breast.

The antennas physically close to a specific antenna are then identified based on both antenna proximity and the strength of the correlation between signals from proposed neighbours. A skin estimate is obtained by generating a weighted combination of the data observed within the SDW at the neighbouring antennas that matches, minimum difference, the specific antenna's SDW signal. Subtracting this estimate from the antenna signal gives the computed breast feature time signal, C_SS, Figure 1 red line.

2.2. Image Formation

There are changes in the dielectric constants as the signal moves through the scanning tank medium, skin and breast tissue. This requires that the information in the 1D $T\_\text{Scatter}_m[\,]$ signal be mapped, i.e., time-shifted, into the round-trip time delay, $\tau_m(x, y, z)$, from all 3D image reconstruction points to each of the M antenna positions around the breast. A Delay-and-Sum (DAS) algorithm is then used to combine the M 1D round trip time delay signals and construct a 3D image, $I[x, y, z]$ [4, 5, 8].

The transit time, T_{ANTENNA}, between the antenna aperture and feed must be estimated, dotted process path in Figure 2, in order to provide the DAS imaging algorithm with the relative position in the time domain signal corresponding to the antenna aperture. Previous studies have estimated T_{ANTENNA} as the peak location in the time domain reflection without any objects present in the scanning tank [10]. In this paper, we used autoregressive modelling of this reflection in the frequency domain signal to determine T_{ANTENNA}, introducing a correction of approximately 2% recently shown to improve image resolution and contrast [11].

2.3. Problem Identification and Proposed Solution

An initial evaluation of the Maklad et al. [7] algorithm's effectiveness in removing the dominant skin reflection signal compares the 2D cross-sections, Figures 3(a) and 3(b), generated from a simulation study. These figures are respectively generated from the 1D time domain signal from a single antenna following ideal skin removal, dashed line path in Figure 2, and computed skin subtraction, solid line path. As will be discussed in detail in Section 3.1, this option is only available with simulated data sets.

Given the broad physical beamwidth of the BAVA-D antenna, the DAS algorithm spreads the 1D round-trip time delay signal, $\tau_m(x, y, z)$, from each of the M antenna positions to all 3D image reconstruction points. This spreading results in the response from a single antenna signal appearing as a series of circular bands in 2D cross-sections, Figure 3, from the 3D image. The intensities of 1D cross-sections are shown below each of the axial, sagittal and coronal images. Selection of these specific cross-sections and the image contrast parameters are detailed in Section 3.2.

Both the 1D cross sections and the 2D images for all three views, axial, coronal and sagittal, show that the intensity in the computed C_SS breast image is significantly reduced compared to the equivalent I_SS image section. We have been investigating approaches to improve the match between computed and ideal image intensities after skin reflection removal. To date, the most significant improvement has been seen after reducing the width of the SDW estimated by the Maklad algorithm. Figure 3(c) shows that deliberately moving the E_T trailing edge to make the SDW 14% shorter has increased the strongest signal intensity of the C_SS image, yellow ring, closer to that of the ideal I_SS gold standard image.

We have interpreted this result as indicating that the current determination of the SDW [7] is consistently over-estimating its width. We offer the following theoretical reasoning of 1) how this over-estimation lowers the C_SS image intensities and 2) why the SDW width over-estimation is occurring.

1. We suggest that this intensity decrease in the C_SS tumour signal is associated with the positions of the maxima and minima chosen to identify the edges of the SDW. Specifically, if the E_T edge is incorrect then the SDW will be calculated from a region where a skin signal overlaps with the breast

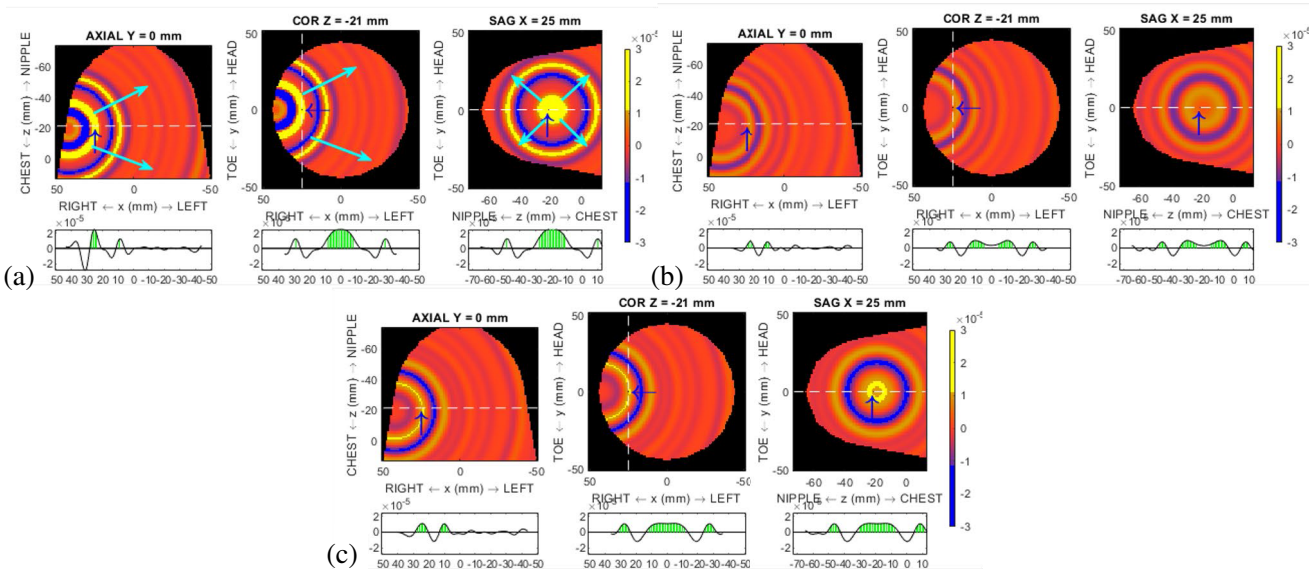

Figure 3. The 1D feature signals from a single antenna display as a series of circular bands in the 2D image cross-sections from the FDTD-SIM study. (a) The two strong feature signals in the I_SS image, outlined in yellow, are very weak from (b) the C_SS image using the original SDW. (c) The intensity of these features begin to be recovered after empirically making the experimental SDW shorter than calculated by the Maklad algorithm.

feature signal. This incorrect positioning implies that minimizing the signal in the automatically chosen SDW will correctly reduce the late components of the skin signal but also lower the intensity of the early breast feature signals in the C_SS images.

2. We suggest that one reason why the existing Maklad algorithm is incorrectly identifying the SDW edges is associated with Gibbs' ringing artefacts known to commonly occur after transforming a limited length frequency data set into the time domain using the direct or inverse discrete Fourier transform, DFT and IDFT respectively [12–15]. In Figure 1, these ringing artefacts are evident both before the leading edge and after the trailing edge of the selected SDW window and will be present throughout the SDW as they are associated with every individual dominant peak present in the time domain signal. The presence of the Gibbs' artefact near 1.2 ns in Figure 1(a) is clearly impacting the determination of the SDW's leading edge position. The narrower frequency bandwidth of the available patient data leads to time domain data with a stronger sinc-function intensity envelope from its Gibbs' ringing, Figure 1(b).

A standard approach to minimize Gibbs' ringing artefacts is to window the finite length frequency data set before transforming into the time domain [12–15]. However, we avoided determining the SDW's width after windowing for two reasons. First, while windowing will reduce Gibbs' ringing artefacts on the skin reflection signal, it will also reduce the intensity present in the tumour signal and widens the skin reflection response, i.e., windowing introduces different SDW-related errors. Second, it is clear from the minimal Gibbs' ringing distortions present in the early part of the tumour response, red lines in Figures 1 and 4 before time 1.2 ns, that these artefacts are reduced as a side effect of subtracting a skin estimate generated from a set of similarly distorted signals from adjacent antennas.

We have explored two new approaches to determining the appropriate width of the SDW to optimize the similarity between the I_SS and C_SS signals and images:

1. Method 1 involved moving the final SDW edge, E_T. We first evaluated the impact of moving E_T as we considered that overestimating SDW by incorrectly placing the leading edge, E_L, was less important since there will be no breast feature signal to distort prior to the arrival of the first skin reflection. The location metrics of peaks and troughs available from the original Maklad algorithm are utilized in this modification. The initial E_T edge of the SDW is selected as the

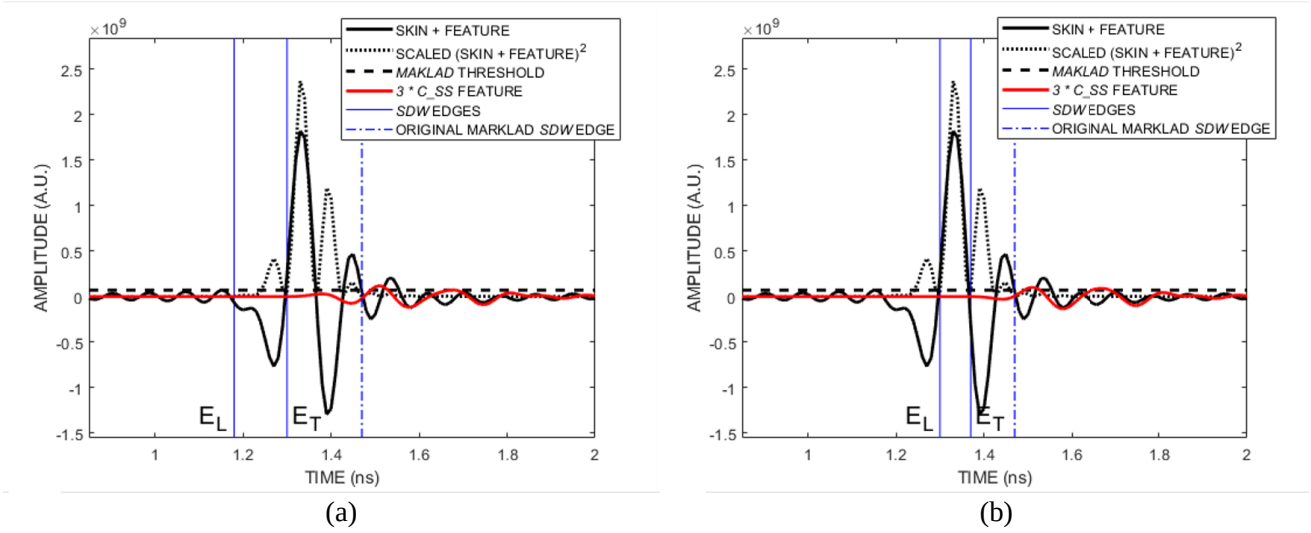

Figure 4. (a) The proposed Method 1 systematically moves the position of E_T in the simulation study until the SDW width is only determined by the location of the skin's significant power peak furthest from the tumour signal. (b) Evaluation of Method 2 involves removing the weaker peaks of the skin reflection until only the strongest power peak determines the SDW width.

trough after the last significant peak, Figure 1(a). The SDW is narrowed by reducing the number of peaks considered as significant when determining the SDW's location, until only the position of the power peak furthest from any tumour signal is used to determine SDW, Figure 4(a).

2. Method 2 SDW modification systematically changes the original power threshold, black dashed line Figure 1, used to determine which peaks are considered significant and contribute to the extent of SDW. This approach modifies both E_L and E_T since the threshold change will result in the dropping of the less intense skin peaks prior to calculating SDW, until only the position of the strongest power peak determines the SDW edges, Figure 4(b). We hypothesize that this will result in a more consistent SDW determination given the final Method 1 SDW peak's skin power levels are expected to be more impacted by Gibbs' ringing artefacts.

We evaluated the proposed SDW modifications in two contexts. First, does the current DAS reconstruction algorithm retain improvements seen in the individual 1D signals in the final 3D images? Second, the Gibbs' ringing artefacts are distorting all parts of the skin signal, and that distortion is specifically related to the characteristics of each individual antenna. Therefore, to better determine the generalizability of the approach, we investigated the sensitivity of improvements in the image formed from a single reflection, as well as the images created by summing 5 signals containing strong tumour responses and the responses of a full dataset.

3. AVAILABLE DATA SETS AND CONSISTENT IMAGE DISPLAY ACROSS STUDIES

In this section, we first identify the simulation and patient data used in this study, and detail how the image display was configured allow a consistent comparison between TSAR images from different reconstruction paths.

3.1. Available Data Sets

An earlier study provided anonymized TSAR scan, RIGHT_BREAST, of a patient's right breast (UCalgary Conjoint Health Research Ethics Board (E-24098)) [4, 5]. This data set is limited to the range 860 MHz to 4.5 GHz given experimental and patient breast characteristics [16]. A gold standard image generated after an ideal skin subtraction is required to study the performance of an algorithm that

computes the removal of the skin reflection. However, a gold standard TSAR patient image is difficult to obtain since the tumour-free case is unlikely to be available for a specific patient. In addition, registration issues make it difficult to use higher resolution MRI and X-ray studies to estimate a gold standard image given the changes in breast shape resulting from these techniques' different physical manipulations [16].

A compromise is to generate simulation studies, referred to as FDTD-SIM, using a commercial finite-difference time-domain (FDTD) program [17]. Reflections are simulated from a breast model consisting of skin, fat and a tumour, Model A, immersed in a tank of canola oil ($\varepsilon_r = 2.5$, $\sigma = 0.04\,\mathrm{S/m}$). The illumination generated by a BAVA-D antenna is calculated as part of the model rather than being than being provided as an estimate [4, 8, 9, 18]. Simulated reflections are also performed with a breast model that consists of skin and fat, Model B, as well as from an empty scanning tank without a model present, Tank signal C.

Subtracting the reflections from Model A and Model B is referred to as ideal skin subtraction, I_SS. This generates the gold standard breast feature reflection, i.e., reflection from the tumour alone, dashed line path in Figure 2. Subtracting the reflections without a model present from the reflections obtained from Model A produced a skin + feature signal. This signal is passed to the skin subtraction algorithm, solid line path in Figure 2, to produce the required computed skin subtraction, C_SS, breast feature signal. The Tank signal C signal can be processed, dotted line path in Figure 2, to provide the transit time estimate, T_{ANTENNA}, of the antenna needed by the DAS algorithm to correctly position the 1D time domain signal information in the 3D image scatter space [10, 11].

3.2. Modifications to the DAS Image Display Format

We made the following modifications to the way images which have been displayed in our previous TSAR studies to provide consistent comparison of images across a variety of reconstruction processes. This follows the suggestions in [11] which evaluated different approaches to calculate the TSAR transit time T_{ANTENNA}:

- To provide consistency with later figures, the axial, sagittal and coronal slice selections for the single antenna images were made equal to the location of the highest intensity voxel in the corresponding complete image, i.e., from a combination of all preprocessed antenna time domain signals.
- The highest intensity pixel in each slice has been coloured black and its location made more obvious amongst any image clutter by a black arrow.
- The white dotted lines show the 2D locations of the 1D cross-sections displayed below the images. The green vertical lines in these 1D cross-sections indicate the position of pixels with intensity greater than 50% of the scatter plot's maximum positive intensity.
- The image colour range was normalized to $[-C, +C]$, $C = \max\{\mathrm{I\_SS_{MAX}}, abs(\mathrm{I\_SS_{MIN}})\}$, to ensure a constant colour map entry for zero-valued pixels, and to allow a consistent qualitative comparison of the relative intensities of the I_SS and C_SS feature signals.
- To show more clearly the changes in the images, we chose to shade pixels with intensities greater than 38% of the maximum positive intensity, C, or less than 38% of the minimum negative intensity, $-C$, in yellow and blue, respectively.

4. RESULTS

In this section, we first evaluate the two proposed SDW-identification algorithms to determine whether improvements could be seen in images formed with single signals from the simulated and patient data. We then determined whether these improvements remained evident in the final images that combined all preprocessed signals.

4.1. SDW Impact on Single Stream FDTD-SIM Images

First, the largest tumour reflection is determined following ideal skin subtraction, I_SS. Next, an image is formed with this signal, Figure 5, This process is repeated at the same antenna location for signals

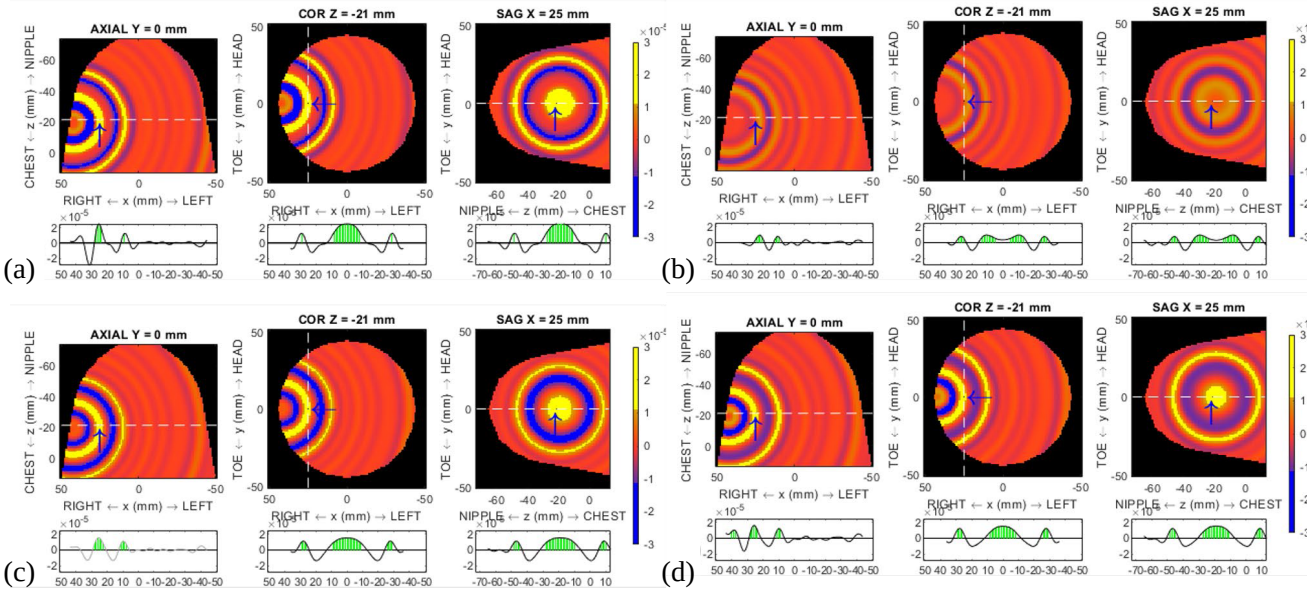

Figure 5. The intensity in the 1-stream image is considerable stronger in (a) following ideal skin subtraction than (b) following computed skin subtraction using the original Maklad SDW width determination. Using either (c) Method 1 or (d) Method 2 approaches to determine the SDW width boosts the signal intensity, generating a better match to the ideal signal.

where the computed skin subtraction, C_SS, has been obtained with different variations on the SDW and comparison 1D cross sections created, Figure 6.

Comparing Figure 5(a), ideal skin subtraction, and Figure 5(b), computed skin subtraction, images show that using Maklad SDW limits causes an equivalent loss of intensity across the axial, coronal and sagittal cross sections of the single stream image. Figures 5(c) and 5(d), Method 1 and Method 2 respectively, show similar enhancements in image intensities.

A more detailed analysis of the impact of SDW changes on tumour and breast feature responses can be obtained by examining the cross sections, dashed white lines, through the tumour and breast feature responses. Figure 6(a) shows cross sections extracted from the axial 2D images of the FDTD-SIM study. Specifically, the SDW width is decreased by changing the position of the E_T edge via Method 1. There is considerable difference in the intensity of the ideal I_SS, black line, and the original Maklad C_SS response, red line, in the region located from 10 mm to 44 mm on the patient's right.

The fact that these changes occur over more than 30% of the data to be used in the complete image reconstruction provides evidence of the considerable impact that the current weighting coefficients determined by the Maklad algorithm will have on the resulting time domain signals. As the SDW width to be minimized by Method 1 is reduced, the C_SS feature grows in intensity with its peaks moving closer to the ideal I_SS peak positions, indicating that the SDW weighting coefficients are losing their distorting impact on the internal breast features. Removing the 3 significant peaks from the SDW closest to the breast feature signal generates a 1D C_SS signal, green line, closest to the ideal I_SS gold standard, black line.

Figure 6(b) shows the changes as the SDW width is decreased using Method 2, equivalent to increasing the Maklad peak selection threshold, dashed black line in Figure 4. As with Method 1, the C_SS signal increases in intensity as SDW decreases in size. Now the better approximation of the I_SS signal shape occurs when only the main skin reflection determines the SDW width, green line. While the two proposed SDW determination methods provide similar C_SS estimates, Method 2 exhibits less evidence of potential residual skin reflection distortion overlaying the early part of the breast feature signal (see Figure 6(a)). This difference in image cross sections is reflected in the time domain signals, Figure 4, where the level of residual skin components remaining on the tumour signal, red line, within the original Maklad SDW is higher for Method 1 than Method 2.

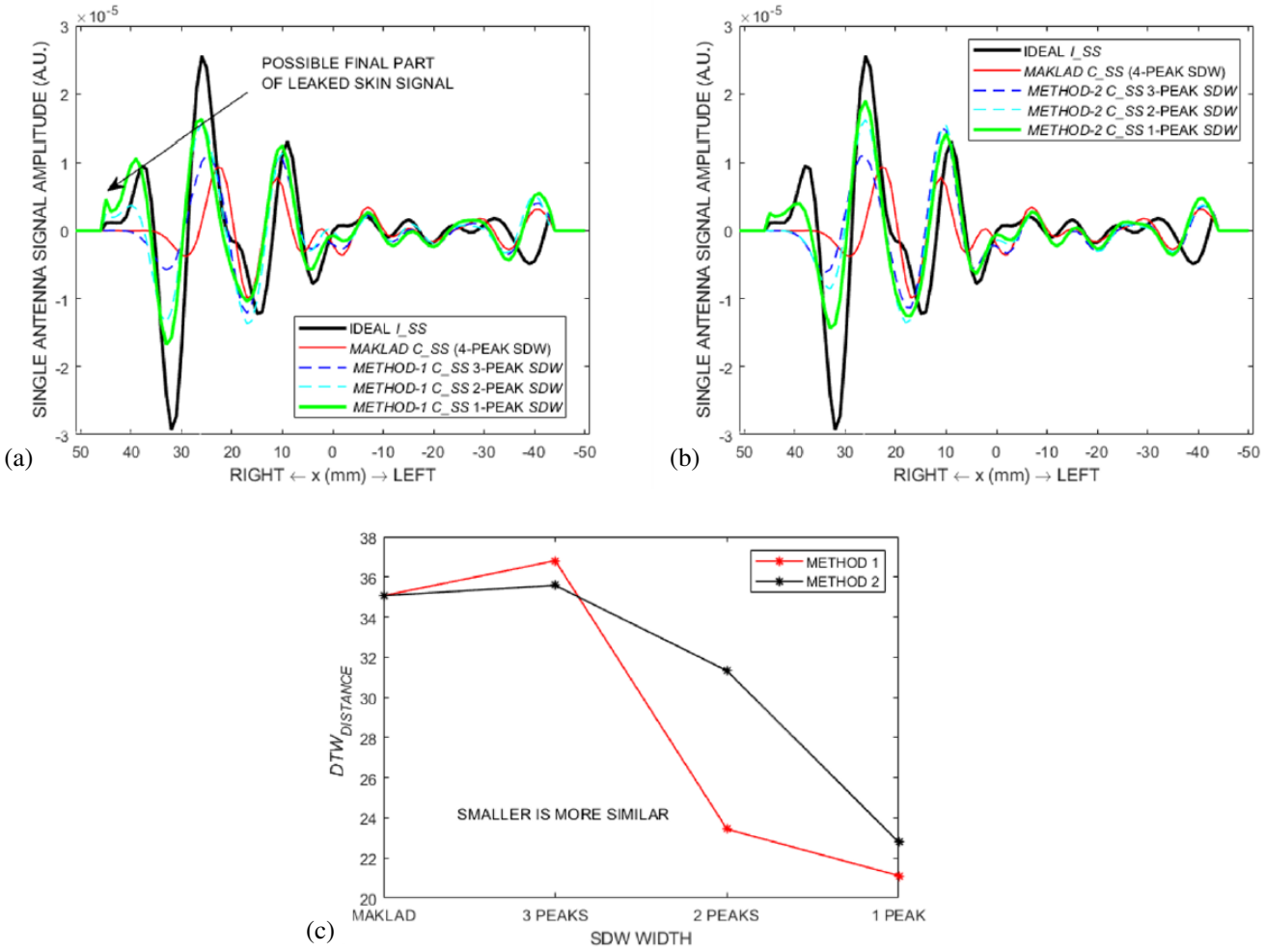

Figure 6. As the SDW to be minimized narrows using (a) Method 1 and (b) Method 2, the C_SS axial cross-section of the breast feature signal grows in intensity and better approximates the ideal I_SS cross-section. (c) Using the dynamic time warping distance, $\mathrm{DTW}_{\mathrm{DISTANCE}}$, smaller-is-better metric, the similarity between the I_SS and computed C_SS cross-sections improves by nearly a factor of 2 when replacing the existing Maklad SDW with either of the two proposed techniques.

Given the considerable differences in the cross-sections as the SDW width is decreased, we have chosen to use the dynamic time warping distance, $\mathrm{DTW}_{\mathrm{DISTANCE}}$, metric to quantitatively measure the level of similarity between the ideal, I_SS, and computed, C_SS, signals, Figure 6(c) [19–25]. The $\mathrm{DTW}_{\mathrm{DISTANCE}} = \mathrm{dtw}(\mathrm{signal1},\ \mathrm{signal2})$ algorithm is appropriate for determining the similarity between two signals when experimental distortions are sufficiently severe that classical comparison approaches, e.g., cross-correlation, fail. DTW generates time-warped versions of the data streams, signal1 and signal2, by duplicating elements in each stream in a recursive manner until the sum of the Euclidian distances between corresponding points in the stretched streams is smallest [19]. The smaller is better, $\mathrm{DTW}_{\mathrm{DISTANCE}}$ metric shows a near doubling of similarity between I_SS and C_SS for the proposed narrowed SDW widths compared to the original Maklad width determination.

4.2. SDW Impact on Single Stream Patient Images

The previous section compared how the two new different approaches to shorten SDW improved the FDTD-SIM breast feature signal from a single antenna. In this section, we explore the degree these two methods change the C_SS signal of the patient data given that there will be different features

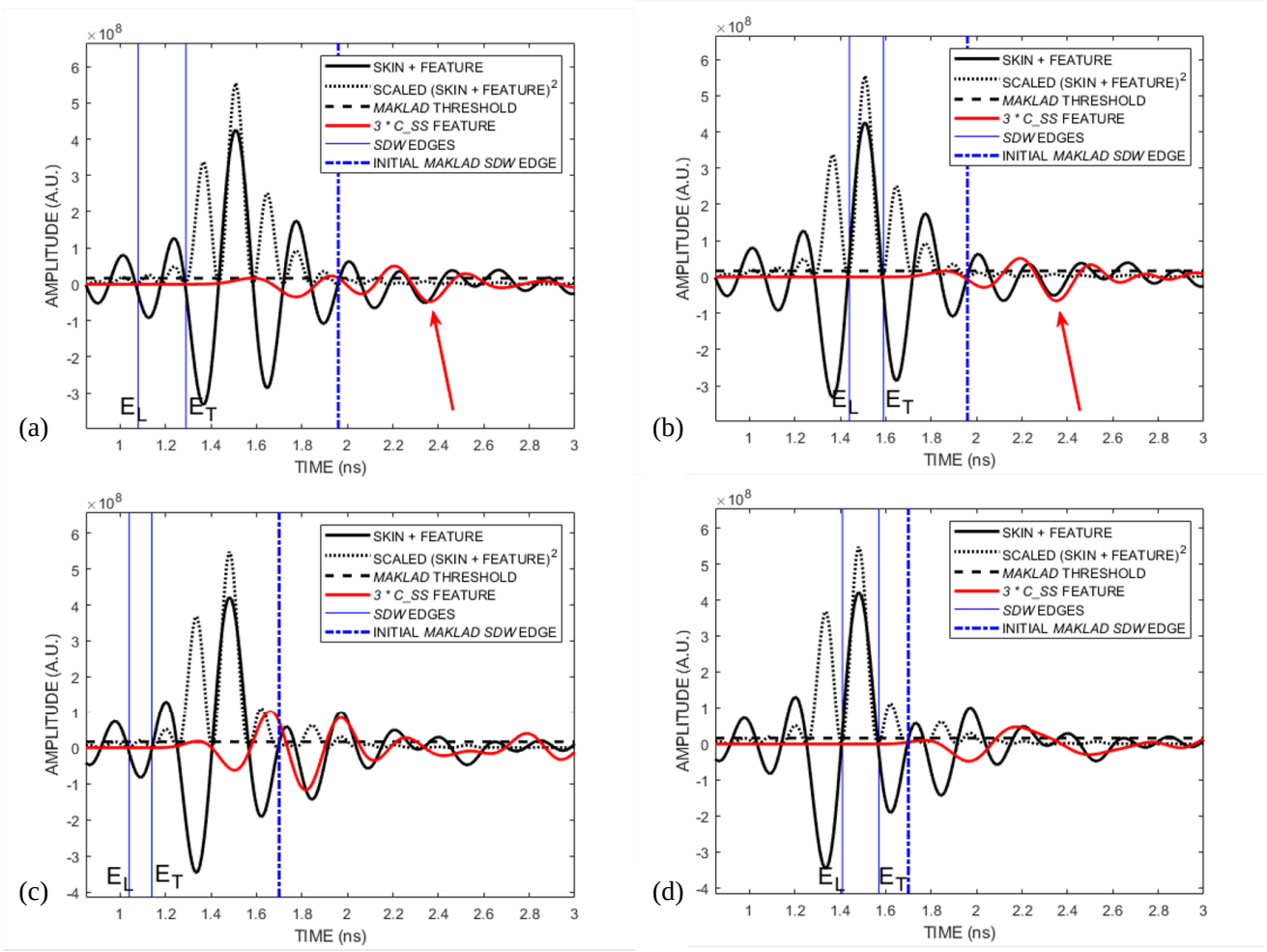

Figure 7. (a) The proposed Method 1 systematically moves the position of E_T in this patient study until the SDW width is only determined by the location of the skin's significant power peak furthest from the tumour signal. (b) Evaluation of Method 2 involves removing the weaker contributions of the skin reflection until only the strongest power peak determines the SDW width. The differences between the residual skin reflections between the two methods is much stronger in this patient study than with the FDTD-SIM study, Figure 4. In addition, unlike the FDTD-SIM study, the skin reflection signal from another location on the breast causes significantly different SDW width locations for the initial Maklad approach, dash-dotted blue line, and for (c) Method 1. In contrast, (d) Method 2 provides a more consistent SDW determination at both breast locations.

within a human breast, the presence of experimental noise and an anticipated range of skin reflection characteristics at different physical locations around the breast.

The computed tumour time signals, red line, and SDW edge locations, blue lines, for an antenna from the patient RIGHT breast study are shown in Figures 7(a) and 7(b) for Method 1 and Method 2 approaches respectively. The corresponding information for the Maklad algorithm is shown in Figure 1(b). Figures 7(c) and 7(d) show the time signals and SDW edge locations for a different antenna for Method 1 and Method 2.

The patient SDW, Figure 1(b), is different than the SDW from the FDTD-SIM study, Figure 1(a), specifically the experimental skin reflection shows more peaks within the SDW. A component of the changed peak shapes may be a result of the true breast skin having a more complex structure than the FDTD-SIM simulated skin. However, we interpret the shape of the amplitude variation (sinc-like envelope) of the additional peaks as more indicative of an increased level of Gibbs' artefacts associated

with the narrower and sharper cutoff of the frequency bandwidth available because of individual breast characteristics, only up to 4.5 GHz. While larger in size, we still expect these artefacts to be removed/reduced as a side-effect of suppressing the true skin reflection as discussed earlier.

From the time domain signal in Figure 1(b), it can be seen that there is no residual skin reflection signal present on the calculated tumour signal, red line, within the SDW chosen using the original Maklad limits. However, skin reflection removal has left the tumour signal suppressed for the 0.3 ns immediately after the SDW trailing edge, E_T, at 2 ns.

Comparing Figures 7(a) and 7(b) shows that, as with the FDTD-SIM study, Method 1 leaves a higher level of unsuppressed skin reflection within the original Maklad SDW than Method 2 while providing an overall increase in tumour signals. Despite the presence of unsuppressed skin reflections, the Method 1 computed tumour signal, red lines remains similar after 1.95 ns with Method 2 although Method 2 provides a slightly higher tumour signal intensity at 2.35 ns, arrows.

Corresponding image cross-sections are shown in Figures 8(a), 8(b), and 8(c). The suppression of the tumour signal by the Maklad SDW is echoed by the lower overall intensity in the Figure 8(a). In Figure 8(b) and 8(c) images, the breast feature signals closest to the skin on the right side of the image have increased in intensity. The increase in intensity for Method 2, Figure 8(c), extends to breast feature signals further from any residual skin reflection that might extend beyond the trailing edge, E_T, of the shortened SDW. This again indicates the global impact of the original Maklad weighting coefficients generated from an over estimated SDW width seen with the simulated studies is repeated in patient studies.

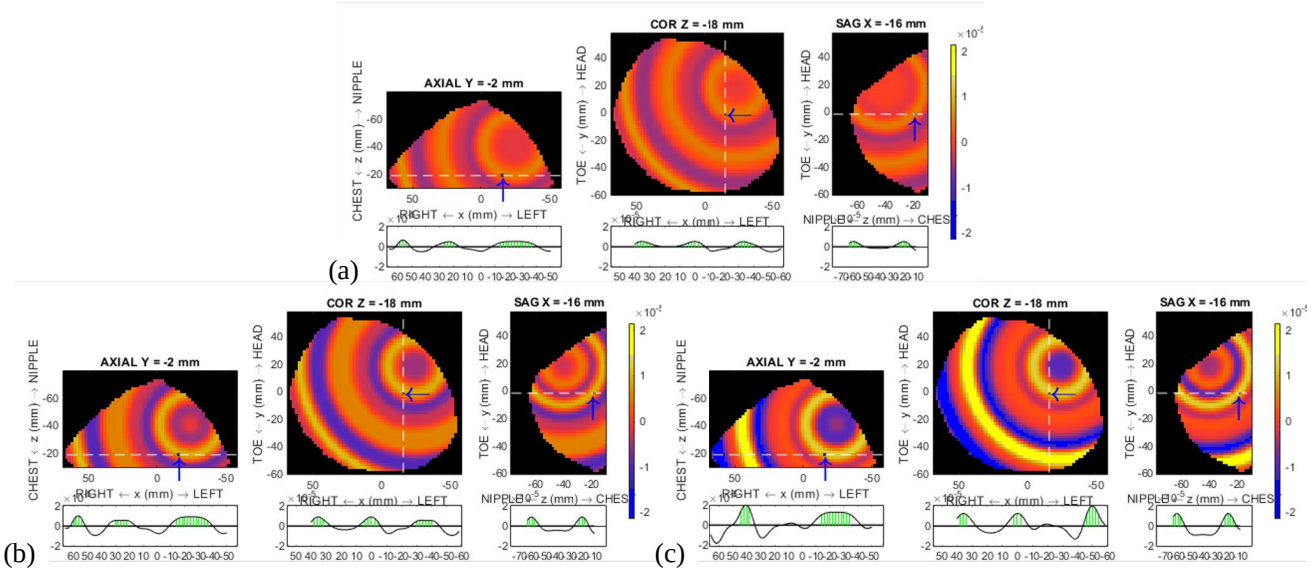

Figure 8. (a) One-stream images from patient using the Maklad SDW. (b) There is a general boost in intensity when SDW is determined using Method 1. (c) There is a further boost in signal intensity down the full data stream when SDW is determined using Method 2. Corresponding time signals and SDW are shown in Figures 1(b), 7(a) and 7(b).

Unlike the FDTD-SIM study with its simulated skin, moving the microwave antenna around the breast produces skin reflection signals with different SDW width locations, c.f. Figures 7(a) and 7(b) with Figures 7(c) and 7(d). The strong Gibbs' ringing artefacts causes Method 1 to select a SDW, Figure 7(c), far from the original trailing edge, dashed blue line, leaving strong skin reflections that extend into and boost the tumour signal intensity above that seen with Method 2, Figure 7(d). In contrast, Method 2 selects a similar SDW position and width for both antenna positions.

As discussed earlier, ideal skin subtraction images are not available with patient studies. Therefore, an equivalent similarity metric to FDTD-SIM Figure 6(c) cannot be generated.

4.3. SDW Impact of the All-Streams Images

This section attempts to answer the question, "*Are the advantages of boosted tumour signals with the new SDW determination approaches noted in a single antenna signal repeated as multiple antenna signals are combined by the DAS algorithm?*"

Figure 9 shows all-stream images created with the complete set of preprocessed data for the FDTD-SIM study, with Figure 9(a) the gold-standard I_SS images. Using the original SDW, Figure 9(b), shows a reduction in intensity, of the positive response in the image. The main image peak, enhanced in yellow, is widened in all three cross-sections. In addition, there is an increase in negative intensity components, enhanced in blue, especially in the coronal and sagittal cross-sections. Suppressing skin reflections using the best SDW from Method 1, Figure 9(c), increases the maximum positive intensity and decreases the maximum negative intensity features, closer to that of the standard I_SS image. Similar intensity increases are seen in Figure 9(d), best SDW by Method 2, with further suppression of the incorrect negative intensity feature. Both of the shorter SDW approaches show a higher resolution, i.e., narrower, main feature compared to images using the original Maklad SDW to suppress skin reflections.

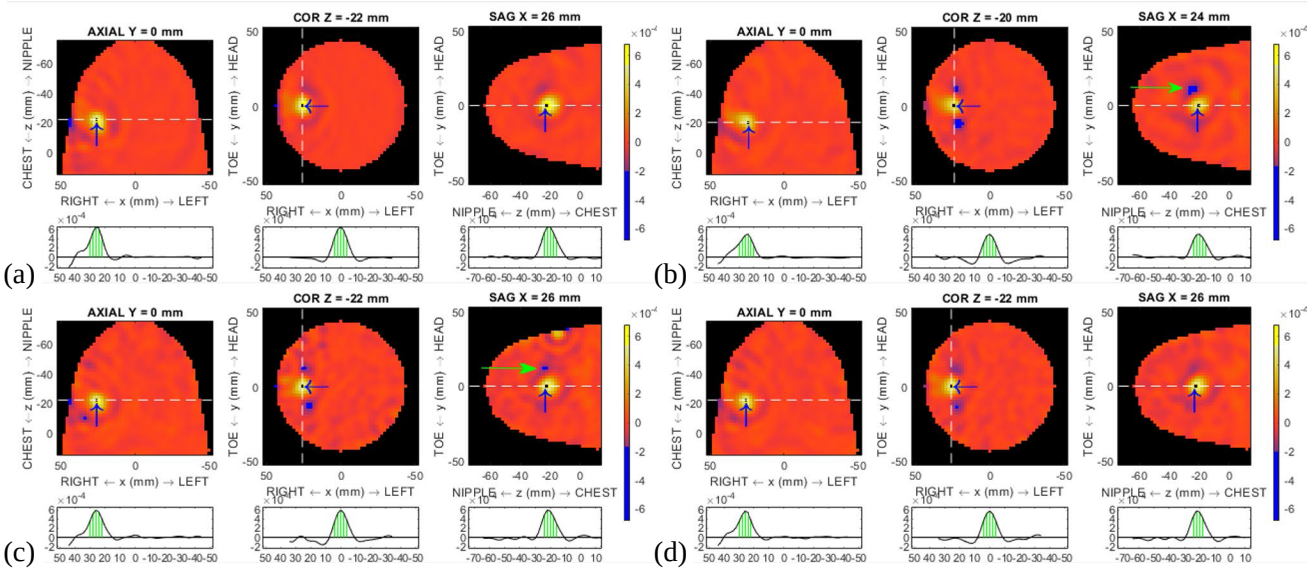

Figure 9. (a) The FDTD_SIM I_SS image has a brighter, narrower main feature, enhanced in yellow, and no strong negative intensity features, enhanced in blue, compared to (b) the C_SS image generated using the original SDW width. (c) Using the best SDW from Method 1, reduces the background peak intensity and narrows and boosts the main feature. (d) The improvement in the main feature intensity and shape and a further reduction in the negative feature intensity occurs in both axial and sagittal cross-sections with SDW determined by Method 2.

Figure 10 uses the dynamic time warping distance, $\text{DTW}_{\text{DISTANCE}}$, smaller-is-better metric, to determine the similarity between the I_SS and computed C_SS FDTD-SIM cross-sections as images are generated with 1 and 5 strong tumour reflections, as well as from all available data. Similarity between I_SS and computed C_SS increases as the SDW width decreases and as more signals are incorporated into the images. The similarity improves by nearly a factor of 2 for both the 1 stream and 5 stream images when replacing the existing Maklad SDW with either of the two proposed techniques. The smaller increase in similarity in the all-stream images is to be anticipated. When combined within the DAS reconstruction algorithm, many of the 140 signals destructively interfere with other signals to suppress the background clutter rather than constructively interfere to enhance the tumour signal. This automatically makes the late parts of the cross-sections very similar, implying that decreases in the $\text{DTW}_{\text{DISTANCE}}$ metric are reflecting localized improvements in the similarity occurring in a small portion of the noisy cross-section that contains the tumour.

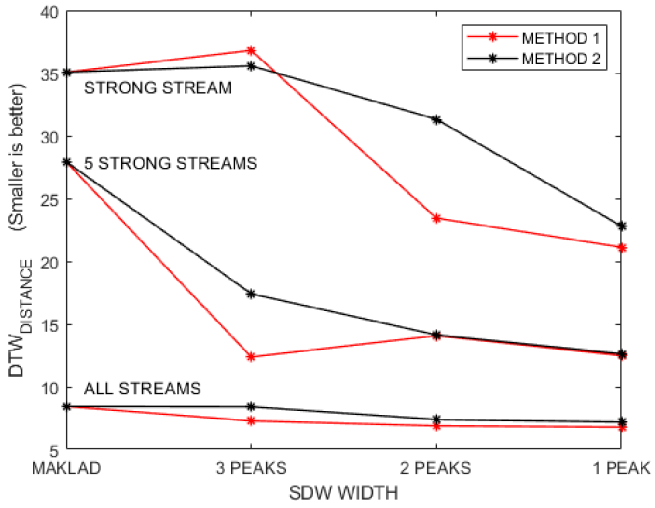

Figure 10. The dynamic time warping distance, $\text{DTW}_{\text{DISTANCE}}$, smaller-is-better metric is used to show changes in the similarity between the I_SS and computed C_SS cross-sections as the SDW width is modified and more antenna time signals are combined into the DAS images. Similarity improves by nearly a factor of 2 when either 1 or 5 strong data streams have skin reflections suppressed by either of the two proposed techniques rather than the existing Maklad SDW approach. The background clutter away from the tumour is greatly reduced when all data streams are combined so that changes in the $\text{DTW}_{\text{DISTANCE}}$ metric now correspond only to the few pixels on the more resolved tumour signal.

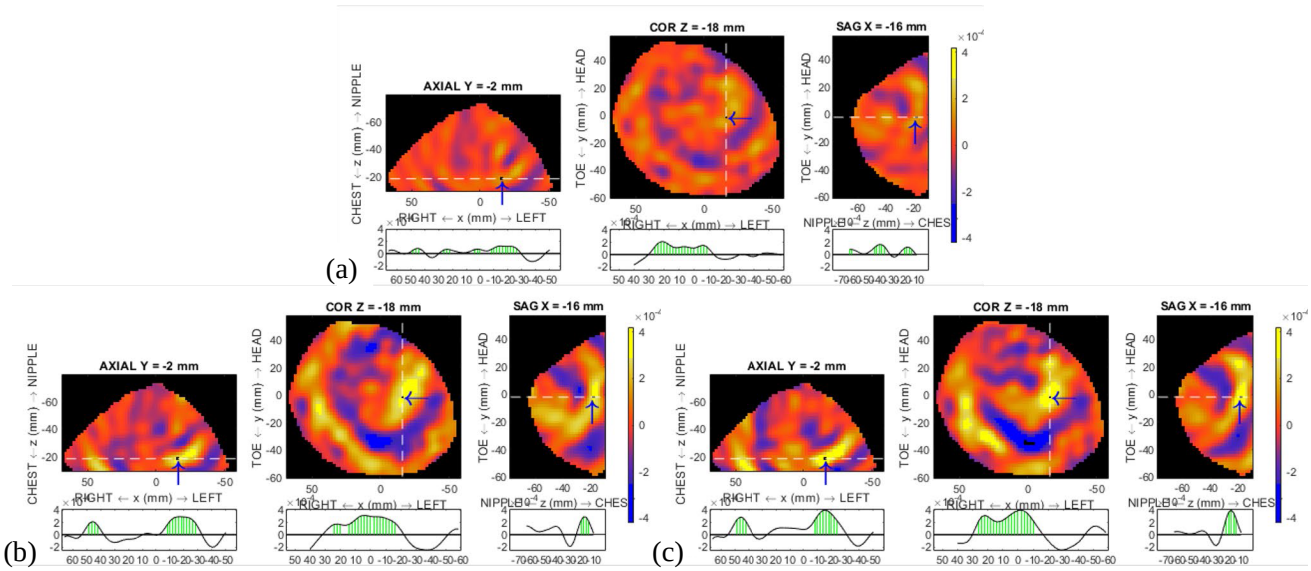

Figure 11. (a) TSAR right breast study using the original SDW. (b) The Method 1 SDW suppression show significant intensity increases in all image sections. (c) As with the one-stream images, Figure 7 the Method 2 images using all preprocessed data show a further increase in intensity when a SDW based only on the narrow main peak is used to minimize the dominant skin reflection during patient studies.

As discussed earlier, there are no gold standard images available for patient studies. Therefore, only a comparison between the C_SS images generated by the different SDW selection processes is shown in Figure 11. The improvements in intensity for shorter SDW seen for the patient one-stream studies, Figure 8, are repeated for the patient images after all preprocessed antenna signals have been

summed. The patient image using the original Maklad SDW, Figure 11(a), is half the intensity of the Method 1 image, Figure 11(b). As with the one-stream study, there is a further increase in intensity with Method 2, Figure 11(c).

We suggest that the greater range of contrast between strong positive and negative features in the physical breast images combined with many low-resolution features is the reason that the changes in the patient images appear more visually significant with a smaller SDW than seen in the simulated FDTD-SIM study, Figure 10.

4.4. Comparison of Proposed SDW Selection Techniques

We have demonstrated two new approaches that separately show that narrowing the SDW has the potential to improve microwave image quality for both simulated and patient data when compared to the Maklad approach. Both methods have been shown to perform well in suppressing the skin reflection in the simulated study while reducing the distortion this suppression previously had on the early part of the tumour signal. We would anticipate similar improved results with the patient data where a gold-standard result is not available. However, based on the evidence presented in this paper, we recommend the use of Method 2 as the better approach to narrow SDW on the following grounds:

1. Comparison of the skin and tumour signal amplitudes in the time domain (Figures 1, 4 and 7) shows that Method 2 exhibits less evidence of the presence of skin reflections in both the tumour and SDW than Method 1.
2. Unlike the idealized simulation study where all skin reflections will be generated essentially identical, physical skin characteristics will change as the antenna moves around the breast. As hypothesized, Figure 7 shows that Method 2 provides a more consistent estimate of the SDW width and position from different antenna orientations than Method 1.
3. Differences 1 and 2 would be reduced by boosting the Maklad power threshold used to identify the significant peaks used to determine SDW, but in the limit that would make Method 1 equivalent to Method 2.
4. Despite these differences, Method 1 results remain consistent with the results from Method 2 after all individual antenna signals are combined into a final image. We attribute this to (a) the DAS algorithm performing a constructive and destructive summation across all antenna signals, thus reducing any remaining error present in the early part of any one individual antenna signal for any given SDW determination, and (b) the imaging region is limited to the breast region after the second skin boundaey, which reduces impact of residual signals remaining inside the original SDW after applying Method 1.

5. CONCLUSION

Low-power, non-ionizing, microwave imaging techniques for breast cancer monitoring offer advantages over X-ray and MRI imaging. A major problem in successful microwave imaging is the removal of the skin reflections given the skin generates a reflection that dominates over the weaker reflections from multiple small features deeper inside the breast. The current skin removal algorithm attempts to identify the skin dominant window, SDW, containing the full skin reflection, and then subtracts a skin estimate based on a weighting of local neighbourhood antenna signals to minimize the signal within the SDW.

We have shown that the Maklad weighting of neighbourhood signals also reduces the breast feature signals due to their partial overlap near the SDW final boundary. This in turn lowers the contrast in the final image. We have proposed two different SDW selection approaches, comparing them with the original approach applied to simulated and patient data using Tissue Sensing Adaptive Radar (TSAR) as the application platform. Method 1 selects the part of the skin reflection furthest from the breast feature signal to provide a narrower SDW when minimizing the skin signal. Method 2 minimizes a SDW based on the narrow main peak of the skin signal. Both approaches provide improved reduction of reflections over the first 30% of the breast signal compared to the original SDW selection process. Despite the similar results, we offered reasons why Method 2 should be the preferred method when

selecting a narrower SDW to generate an improved skin reflection estimate while minimizing breast feature distortions.

However, Method 1 should not be completely dismissed as a potential approach to validly enhance the tumour signals for the following reason. The limited frequency range will introduce Gibbs' ringing artefacts into both the skin reflection and breast feature time domain signals; the later possibly not strongly apparent as the breast signal amplitudes were reduced using the previous computed skin suppression approach. Therefore, future work is needed to determine whether the increased level of 'unsuppressed skin reflections' with Method 1 mentioned in Section 4 should be interpreted in a different manner. "*Are these signals actually Gibbs' distortions on the internal breast feature reflections after their intensity has been boosted by the new SDW determination methods and made more apparent above the original background clutter?*" A new route to enhancing TSAR images is opened up if this hypothesis is correct.

We have successfully introduced the dynamic time warping distance measure, $\mathrm{DTW}_{\mathrm{DISTANCE}}$, as a metric to quantify near-field microwave image improvement. This leads to the hypothesis that there may be advantages if the current algorithm to produce a skin reflection estimate is replaced by applying dynamic time warp averaging techniques, DTWA, [20–25] to combine signals from the local neighbourhood of antenna.

MATLAB code and representative data are available by contacting the authors.

ACKNOWLEDGMENT

This work was supported in part by the Natural Sciences and Engineering Research Council (NSERC) of Canada, and by the Department of Electrical and Software Engineering, Schulich School of Engineering, University of Calgary. The authors thank I. DasGupta for discussions on how various preprocessing techniques impact the appearance of TSAR images. The authors thank the reviewers whose well-directed comments have led us to a major revisualization of this paper.

REFERENCES

1. O'Loughlin, D., M. O'Halloran, M. Glavin, J. Martin, E. Jines, and M. A. Elahi, "Microwave breast imaging: Clinical advances and remaining challenges," *IEEE Transactions on Biomedical Engineering*, Vol. 65, No. 11, 2580–2590, Nov. 2018.
2. O'Halloran, M., M. Glavin, and E. Jones, "Performance and robustness of a multistatic MIST beamforming algorithm for breast cancer detection," *Progress In Electromagnetics Research*, Vol. 105, 403–424, 2010.
3. Winters, D. W., J. D. Shea, E. L. Madsen, G. R. Frank, B. D. van Veen, and S. C. Hagness, "Estimating the breast surface using UWB microwave monos," *IEEE Transactions on Biomedical Engineering*, Vol. 55, No. 1, 247–256, 2008.
4. Curtis, C. and E. Fear, "Beamforming in the frequency domain with applications to microwave breast imaging," *IEEE 8th European Conference on Antennas and Propagation (EuCAP))*, 72–75, The Hague, Netherlands, 2014.
5. Curtis, C., "Factors affecting image quality in near-field ultra-wideband radar imaging for biomedical applications," University of Calgary, Calgary, 2015.
6. Bond, E. J., X. Li, S. C. Hagness, and B. D. van Veen, "Microwave imaging via space-time beamforming for early detection of breast cancer," *IEEE Transactions on Antennas and Propagation*, Vol. 8, No. 51, 1690–1705, 2003.
7. Maklad, B., C. Curtis, E. C. Fear, and G. G. Messier, "Neighborhood-based algorithm to facilitate the reduction of skin reflections in radar-based microwave," *Progress In Electromagnetics Research B*, Vol. 39, 115–139, 2012.
8. Kurrant, D., J. Bourqui, and E. Fear, "Surface estimation for microwave imaging," *Sensors*, Vol. 17, 1658, 2017.
9. Garrett, J. and E. Fear, "A new breast phantom with a durable skin layer for microwave breast imaging," *IEEE Transactions on Antennas and Propagation*, Vol. 63, No. 4, 1693–1700, 2015.

10. Bourqui, J., D. Kurrant, B. R. Lavoie, and E. C. Fear, "Adaptive monostatic system for measuring microwave reflection from the breast," *Sensors*, Vol. 18, No. 5, 1340, 2018.
11. Smith, M. R., I. Dasgupta, and E. Fear, "New resolution enhancement approach for tissue sensitive adaptive radar (TSAR)," *32nd Irish Signals and Systems Conference (ISSC 2021)*, IEEE, Athlone, Ireland, 2021, https://doi.org/10.1109/ISSC52156.2021.9467874.
12. Harris, F. J., "On the use of windows for harmonic analysis with the discrete fourier transform," *Proceedings of the IEEE*, Vol. 66, 51–83, 1978.
13. Smith, M. R., "FFT — fRISCy Fourier transforms," *Microprocessors and Microsystems*, Vol. 17, No. 9, 507–521, 1993.
14. Liang, Z. P., F. E. Boada, R. T. Constable, E. M. Haacke, P. C. Lauterbaur, and M. R. Smith, "Constrained reconstruction methods in MR imaging," *Reviews of Magnetic Resonance in Medicine*, Vol. 4, No. 2, 67–185, 1992.
15. Mitra, S. K., *Digital Signal Processing: A Computer-based Approach*, McGraw Hill, 1998.
16. Curtis, C., R. Frayne, and E. Fear, "Using X-ray mammograms to assist in microwave breast image interpretation," *International Journal of Biomedical Imaging*, 2012, doi.org/10.1155/202/235380.
17. SPEAG, "The Finite-Difference Time-Domain (FDTD) technique," [Online], 2020 [cited 2020 December 1]. Available from: speag.swiss/products/semcad/modules/what-is-fdtd/.
18. Bourqui, J., M. Okoniewski, and E. C. Fear, "Balanced antipodal Vivaldi antenna with dielectric director for near-field microwave imaging," *IEEE Transactions on Antennas and Propagation*, Vol. 58, No. 7, 2318–2326, 2010.
19. Mathworks, "DTW — Distance between signals using dynamic time warping," [Online], 2021 [cited 2021 3]. Available from: mathworks.com/help/signal/ref/dtw.html.
20. Petitjean, F. and I. Paparrizos, "DBA: Averaging for dynamic time warping," [Online], 2017 [cited 2021 3 1]. Available from: github.com/fpetitjean/DBA.
21. Petitjean, F., K. Ketterlin, and P. Gancarski, "A global averaging method for dynamic time warping, with applications to clustering," *Pattern Recognition*, Vol. 4, No. 3, 678–693, 2011.
22. Schultz, D. and B. Jain, "Non-smooth analysis and sub-gradient methods for averaging in dynamic time warping spaces," *Pattern Recognition*, Vol. 74, 340–358, 2017.
23. Chan, R. S. L., P. Gordon, and M. R. Smith, "Evaluation of dynamic time warp barycenter averaging (DBA) for its potential in generating a consensus nanopore signal for genetic and epigenetic sequences," *International Conference of the IEEE Engineering in Medicine and Biology Society (EMBC'18)*, 4821–2824, IEEE, Honolulu, 2018, https://doi.org/10.1109/EMBC.2018.8512873.
24. Smith, M. R., R. S. L. Chan, and P. Gordon, "Evaluating the accuracy of consensus nanosequencer squiggles generated by dynamic time warp barycentre averaging (DBA)," *IEEE Engineering in Medicine and Biology*, 233–237, IEEE, Berlin, 2019, https://doi.org/10.1109/EMBC.2019.8856460.
25. Smith, M., R. Chan, M. Khurram, and P. Gordon, "Evaluating the effectiveness of ensemble voting in improving the accuracy of consensus signals produced by various DTWA algorithms from step-current signals generated during nanopore sequencing," *PLoS Computational Biology*, Vol. 17, No. 9, e1009350, 2021, https://doi.org/10.1371/journal.pcbi.1009350.